Bioactive Materials 6 (2021) 3396–3410

Contents lists available at ScienceDirect

Bioactive Materials

journal homepage: www.sciencedirect.com/journal/bioactive-materials

3D printed silk-gelatin hydrogel scaffold with different porous structure and cell seeding strategy for cartilage regeneration

Qingtao Li [a,c,f,1], Sheng Xu [a,b,d,1], Qi Feng [a,b,d], Qiyuan Dai [a,b,d], Longtao Yao [a,b,d], Yichen Zhang [a,b,d], Huichang Gao [a,c,d], Hua Dong [a,b,d], Dafu Chen [e,**], Xiaodong Cao [a,b,d,f,*]

[a] National Engineering Research Center for Tissue Restoration and Reconstruction (NERC-TRR), South China University of Technology, Guangzhou, GuangDong, 510641, China
[b] Department of Biomedical Engineering, School of Material Science and Engineering, South China University of Technology, Guangzhou, GuangDong, 510641, China
[c] School of Medicine, South China University of Technology, Guangzhou, GuangDong, 510641, China
[d] Key Laboratory of Biomedical Engineering of Guangdong Province, Key Laboratory of Biomedical Materials and Engineering of the Ministry of Education, Innovation Center for Tissue Restoration and Reconstruction, South China University of Technology, Guangzhou, GuangDong, 510641, China
[e] Laboratory of Bone Tissue Engineering, Beijing Laboratory of Biomedical Materials, Beijing Research Institute of Orthopaedics and Traumatology, Beijing JiShuiTan Hospital, Beijing, 100035, China
[f] Zhongshan Institute of Modern Industrial Technology of SCUT, Zhongshan, Guangdong, 528437, China

ARTICLE INFO

Keywords:
Silk hydrogel
3D printing
Enzymatic cross-linking
Cell aggregate seeding
Cartilage regeneration

ABSTRACT

Hydrogel scaffolds are attractive for tissue defect repair and reorganization because of their human tissue-like characteristics. However, most hydrogels offer limited cell growth and tissue formation ability due to their submicron- or nano-sized gel networks, which restrict the supply of oxygen, nutrients and inhibit the proliferation and differentiation of encapsulated cells. In recent years, 3D printed hydrogels have shown great potential to overcome this problem by introducing macro-pores within scaffolds. In this study, we fabricated a macroporous hydrogel scaffold through horseradish peroxidase (HRP)-mediated crosslinking of silk fibroin (SF) and tyramine-substituted gelatin (GT) by extrusion-based low-temperature 3D printing. Through physicochemical characterization, we found that this hydrogel has excellent structural stability, suitable mechanical properties, and an adjustable degradation rate, thus satisfying the requirements for cartilage reconstruction. Cell suspension and aggregate seeding methods were developed to assess the inoculation efficiency of the hydrogel. Moreover, the chondrogenic differentiation of stem cells was explored. Stem cells in the hydrogel differentiated into hyaline cartilage when the cell aggregate seeding method was used and into fibrocartilage when the cell suspension was used. Finally, the effect of the hydrogel and stem cells were investigated in a rabbit cartilage defect model. After implantation for 12 and 16 weeks, histological evaluation of the sections was performed. We found that the enzymatic cross-linked and methanol treatment SF_5GT_{15} hydrogel combined with cell aggregates promoted articular cartilage regeneration. In summary, this 3D printed macroporous SF-GT hydrogel combined with stem cell aggregates possesses excellent potential for application in cartilage tissue repair and regeneration.

1. Introduction

Articular cartilage injury is a common clinical orthopedic disease caused by aging, obesity, or traumatic mechanical destruction and difficult self-repair [1]. Current treatments for cartilage defects include marrow stimulation, autografts, and matrix-induced autologous chondrocyte implantation (known as MACI). Although these treatments provide short-term benefits in specific subsets of patients [2,3], in many cases they result in fibrocartilage regeneration with inferior mechanical performance and cushioning [4]. Therefore, how to efficiently repair

Peer review under responsibility of KeAi Communications Co., Ltd.
* Corresponding author. National Engineering Research Center for Tissue Restoration and Reconstruction (NERC-TRR), South China University of Technology, Guangzhou, GuangDong, 510641, China.
** Corresponding author.
E-mail addresses: chendafu@jsthospital.org (D. Chen), caoxd@scut.edu.cn (X. Cao).
[1] These authors contributed equally to this work.

https://doi.org/10.1016/j.bioactmat.2021.03.013
Received 21 December 2020; Received in revised form 3 March 2021; Accepted 3 March 2021

cartilage defects remains a significant challenge.

In recent years, hydrogels have been widely used in cartilage defect repair and regeneration because their 3D hydrophilic polymer networks are similar to the articular cartilage extracellular matrix [5,6]. Numerous natural and synthetic hydrogels have been successfully designed to enable cartilage restoration by providing a 3D microenvironment for chondrocytes or stem cells [7]. Many physical characteristics of hydrogels, such as stiffness [8], degradation profile [9], crosslinking density [10], and porous structure [11,12], play a pivotal role in cell behavior regulation and thus influence the efficacy of cartilage regeneration. Traditional dense bulk hydrogels do not meet the requirements for cartilage regeneration [6]. For example, such hydrogels usually have submicron- or nano-sized crosslinking network pores, which impedes the diffusion of nutrients and cellular metabolic wastes across the 3D constructs, drastically inhibits cell settlement and proliferation, and provides insufficient living space for extracellular matrix deposition [13,14]. Furthermore, it is difficult to control stem cells to preferentially differentiate into hyaline-like cartilage because the cellular state is affected in dense bulk hydrogels, especially during long regeneration periods. Therefore, it is critical for hyaline cartilage regeneration to design a novel 3D hydrogel with larger pores in micro- or even macro-scale to optimize the directed differentiation of stem cells.

Porous hydrogels can be fabricated using various approaches, such as freeze drying [15], 3D printing [16,17], microgel assembly [18,19], and porogen-based establishment [20,21]. Among these, 3D printing is a powerful and controllable method with which hydrogels can be printed layer-by-layer following computer-assisted design to form a complex structure. Moreover, 3D-printed hydrogels have shown great potential to meet the mechanical, structural, and biological requirements for cartilage defect repair [16]. Gelatin has suitable rheological properties and thermosensitivity in favor of extrusion-based 3D printing and is widely used in biomedical materials due to its excellent biocompatibility, cell affinity, and biodegradation [22,23]. However, there is still one crucial limitation of using gelatin hydrogels-their poor mechanical integrity [24]. Meanwhile, establishing a macroporous structure within bulk hydrogels may further weaken its physical properties, especially structural stability and mechanical strength [25]. Therefore, it is a significant challenge to produce a mechanically stable 3D printed gelatin hydrogel with a predetermined internal pore structure.

Silk fibroin (SF) is a natural biopolymer that has been successfully used in medicine for decades. In recent years, SF has been recognized as an attractive material for cartilage regeneration because of its remarkable biocompatibility and tailorable mechanical properties [26–29]. More importantly, SF hydrogels can be constructed through either the self-assembly of β-sheets or some chemical reaction [30]. SF was found containing many tyrosine groups, which can be oxidized into covalent dityrosine crosslinks. This enzymatically crosslinked SF hydrogel has many controllable physical and chemical properties, which is advantageous to the repair of various types of tissue [31–33]. Accordingly, the combined use of silk and gelatin to form a biocompatible composite hydrogel suitable for 3D printing can realize the adaptive control of pore structure. In this study, the number of phenol groups on gelatin was increased through tyramine substitution. GT molecules could be rapidly crosslinked with SF molecules under the catalysis of HRP and H_2O_2. SF could act as a structural matrix and provide structural stability by enzymatic cross-linking with gelatin and other SF molecules.

During *in vitro* fabrication and culture of tissue-engineered cartilage, mesenchymal stem cell (MSC) chondrogenesis and chondrocyte phenotype maintenance are influenced by the cell density of the 3D construction [34], cell shape [35], and cell–cell interactions [36]. However, in many cell culture processes of the 3D printed hydrogel, MSCs are seeded directly to the 3D scaffold as a cell suspension. In this situation, most cells drip over the framework through its macropores, which leads to low cell retention and uneven cell distribution [34,37]. Many cells adopt long spindle, flat, and polygonal morphologies when they adhere to fibers of the scaffold [38]. Some specialized cell seeding methods (i.e., spheroid, pellet, and cell aggregate seeding methods) were developed to overcome the above problems [39–41]. Cell aggregates are hundreds of micrometers in size and can self-organize through interaction with many cells [42–44]. In the cell aggregate, the morphology of cells is similar to spherical chondrocytes, which are randomly spaced in the middle zone of articular cartilage [45,46], or like undifferentiated MSCs at a particular stage during limb development [37]. To assemble cells into a 3D scaffold and promote more cell residence and penetration, more cells need to retain their rounded morphology. In this paper, we first developed an agarose hydrogel microarray for preparing cell aggregates and then seeded cell aggregates into the 3D printed SF-GT scaffolds with various pore structures.

In the present study, we attempted to fabricate a new 3D printed SF-GT hydrogel with a specific internal pore structure. The structural properties, mechanical properties, and degradation characteristics of each hydrogel scaffold were investigated. Furthermore, *in vitro* testing was designed to evaluate the tissue engineering cartilage formation. Finally, the *in vivo* therapeutic potential of scaffolds and cell aggregates for cartilage defects was explored.

2. Materials and methods

2.1. Materials

Gelatin (type A, 300 g bloom) was purchased from Sigma Aldrich. Degummed silk was purchased from Simatech Incorporation, China. LiBr, N-(3-Dimethylaminopropyl)-N'ethylcarbodiimide hydrochloride (EDC), N-Hydroxysulfosuccinimide sodium salt (NHS), tyramine hydrochloride, morpholinoethanesulfnic acid (MES), and HRP (300 units/mg) were purchased from Aladdin Chemical Reagent Co., Ltd., China. Methanol and aqueous H_2O_2 solution (30% (w/w)) were purchased from Guangzhou Chemical Reagent Factory, China.

2.2. Preparation of silk-gelatin 3D printing hydrogel scaffold

2.2.1. Synthesis of gelatin-tyramine

Gelatin-tyramine was prepared by combining gelatin and tyramine hydrochloride via carbodiimide-mediated condensation of the carboxyl groups of gelatin and the amino groups of tyramine. Briefly, gelatin powder (10 g) was dissolved in 50 mM MES aqueous solution (500 mL). After the dissolution of gelatin, three different proportions of tyramine, EDC, and NHS were added, and the mixture was stirred at 25 °C for 12 h. The resultant polymer solution was transferred into a dialysis membrane (MWCO: 12000–14000) and dialyzed in deionized water for 4 d. The samples were subsequently lyophilized and stored for further use.

2.2.2. Preparation of silk fibroin solution

The SF aqueous solutions were prepared according to the established method. Briefly, degummed silk was dissolved in 9.3 M LiBr aqueous solution at 60 °C for 4 h. The solution was dialyzed in deionized water for 2 d at 25 °C using a dialysis membrane (MWCO: 3500) to remove the salt. The concentration of the silk fibroin solution was adjusted to 6 wt%, and the solution was stored in a freezer at 4 °C.

2.2.3. Rheological characterization

A rheometer (MCR 350) was used to measure the change of storage modulus G′ and G″ of GT with temperature (temperature range: 4–37 °C, heating rate: 0.5 °C/min) at constant frequency (1 Hz) and constant strain (0.1%). GTs of different substitution degree were dissolved at 15% (w/v) in deionized water, 2.5% (w/v) SF, and 5% (w/v) SF to obtain SF_0GT_{15}, $SF_{2.5}GT_{15}$, and SF_5GT_{15} pregel solutions at 50 °C. The viscosities of the different pregels with varying shear rate (0–1000 s^{-1}) and constant temperature (30 °C) were measured.

2.2.4. 3D printing of scaffolds and hydrogel formation

The 3D bioplotter (Envision TEC, Germany) was used to prepare 3D-printed SF/GT hydrogel scaffolds. HRP with a concentration of 60 U/mL was added to the three pregel solutions prepared in section 2.2.3, and the mixtures were then transferred into printer cartridges. The dosing pressure of the syringe pump was set between 1 and 1.5 bar, and the moving speed of the dispensing unit was set to 10–15 mm/s. The nozzle size was selected to be 200 μm, and the fiber spacing was set to 0.6 mm. The temperature of the cartridge and printing platform were set to 20–30 °C and 4 °C, respectively. Printed scaffolds were immediately transferred into 5 mM H_2O_2 solution and left to rest for 30 min to obtain enzymatically crosslinked hydrogel scaffolds (denoted as E-SF_0GT_{15}, E-$SF_{2.5}GT_{15}$, and E-SF_5GT_{15}). The scaffolds were then transferred into 75% methanol solution for 12 h, after which they were washed with deionized water three times to remove the methanol and obtain the final hydrogels (denoted as EM-SF_0GT_{15}, EM-$SF_{2.5}GT_{15}$, and EM-SF_5GT_{15}).

2.2.5. Analysis of the surface and internal structure of the scaffold

All the 3D-printed hydrogels were observed and photographed by a digital camera (60D, Canon, Japan). Next, the scaffolds were freeze-dried and freeze-fractured in nitrogen. The front and cross section of each scaffold were sputter-coated with a 60 s platinum layer and then observed via a scanning electron microscope (Q25 SEM, FEI, USA).

2.2.6. Fourier transform infrared (FTIR) characterization

The E-SF_0GT_{15}, E-$SF_{2.5}GT_{15}$, E-SF_5GT_{15}, EM-SF_0GT_{15}, EM-$SF_{2.5}GT_{15}$, and EM-SF_5GT_{15} hydrogels were lyophilized, and their infrared absorption spectra were measured by Nicolet, MAGN-IR 760. The test conditions were as follows: the test resolution was 4 cm^{-1}, the number of scans was 64, and the test wavenumber range was 400–4000 cm^{-1}.

2.2.7. Mechanical properties

Compressive mechanical tests were performed using a universal mechanical testing machine (Instron 5967, USA). Before each test, the sample was punched into a cylinder about 10 mm in diameter and 4 mm in height. The compressive loading speed was 1 mm/min, and the pressure stopped when the sample fracture or shape variable reached 90%. The stress–strain curves of hydrogel were obtained, and the compression modulus, toughness, and stress at 90% deformation of hydrogel scaffolds were obtained through calculation. To investigate the shape recovery ability and the antifatigue properties of the hydrogel scaffolds, we performed two kinds of cyclic testing. First, the samples were exposed to nine cycles of ramp force loading and unloading. The loading and unloading rates were 1 mm/min. Second, the samples were exposed to a periodic (1/5 Hz) 50 kPa compressive stress, with more than 800 consecutive cycles performed for each EM-SF_5GT_{15} hydrogel sample.

2.2.8. Analysis of swelling ratio, porosity, and degradation

The five printed scaffolds obtained in Section 2.2.4 were freeze-dried and weighed; this weight was recorded as W_0. The scaffolds were then placed in PBS solution, fully swelled for 4 h, gently wiped with filter paper to remove surface moisture, and weighed; this weight was recorded as W_1. The water absorption rate and swelling ratio were calculated with the following equations:

$$\text{Water absorption rate} = \frac{W_1 - W_0}{W_1} \times 100\%$$

$$\text{Swelling ratio} = \frac{W_1 - W_0}{W_0} \times 100\%$$

The porosity of the scaffold after drying was measured by density balance as follows. First, the weight of the hydrogel after freeze-drying was measured and recorded as w. Second, the dry hydrogel was added to ethanol and placed in a vacuum for 1 h until the scaffold was filled with absolute alcohol. Then the scaffold was taken out, and its surface was gently dabbed with gauze saturated with alcohol. The weight of the scaffold was measured and recorded as w_1. Third, the sample was placed in the density balance. The solution in the density balance was anhydrous ethanol. The weight of the sample was measured and recorded as w_2. The porosity of freeze-dried hydrogel was calculated ($n = 5$) as follows:

$$\text{Porosity} = (w_1 - w)/(w_1 - w_2)$$

The five printed scaffolds obtained in Section 2.2.4 were freeze-dried and weighed, and the weight was recorded as $W1$. Then scaffolds were immersed in PBS solution with pH = 7.4 and transferred to a thermostatic shaker (37 °C, 100 rpm) at a specified time point (1, 3, 5, 7, 9, 14, or 21 d). Samples were freeze-dried, and their weight was recorded as $W2$. The calculation formula of degradation rate was $(W1 - W2)/W1$ ($n = 5$), and degradation curves with time were generated.

2.2.9. Biocompatibility evaluation

Human adipose-derived stem cells (hADSCs cat. No. HUXMD-01001) were purchased from Cyagen Biosciences (Suzhou) Inc. (Suzhou, China), propagated in hADSCs basal medium (HUXMD-90011, Cyagen, Suzhou, China), and incubated at 37 °C, 5% CO_2, and 95% humidity while the culture medium was refreshed every 2 d. The hADSCs were seeded on scaffolds (100,000 cells per scaffold), cell proliferation was detected by using CCK-8 (Dojindo, China), and cell viability was evaluated by the Live/Dead Assay kit (Dojindo, China). Images of live cells (stained in green by calcein acetoxymethyl) and dead cells (stained in red by propidium iodide) were captured by a confocal microscope (TCS-SP8, Leica, Germany). Moreover, the cell morphology of hADSCs seeded on the scaffold was also observed using an SEM.

2.3. Hydrogels with different porous structures and different cell seeding strategies

2.3.1. 3D-printed EM-SF_5GT_{15} hydrogel with through holes or staggered holes

For the preparation of 3D-printed hydrogel with through holes, there were two circulation layers: the deflection angle of the first layer was 0°, and that of the second layer was 90°. For the preparation of 3D-printed hydrogel with staggered holes, there were four circulation layers: the deflection angles of the layers were 0° for the first layer, 90° for the second layer, 0° for the third layer, although the deposited fiber was shifted 0.3 mm in the Y direction compared to the first layer, and 90° for the fourth layer. The microarchitecture of the hydrogel was observed by SEM and synchrotron radiation−microcomputed tomography (SR-μCT, XTV160H, X-TEK, UK). In addition, the porosity and liner cyclic loading tests were performed.

2.3.2. Preparation of hADSC aggregates

Cell aggregates were prepared by dropping a cell suspension on an agarose microwell array which was obtained by pouring hot agarose solution on a PDMS microwell mold. The agarose microwell arrays were transferred to 96-well plates, and then 20 μL cell suspensions (of three different cell concentrations: 10^6, 2×10^6, and 4×10^6 cells/mL) were poured into each well. After that, 150 μL medium was added to each well, and the plates were carefully transferred into the incubator. After 24 h of incubation, the cell aggregates were gently blown with 200 μL pipette tips, and then the medium of each well was transferred into a centrifuge tube for centrifugation (1000 rpm, 5 min) to separate the medium and cell aggregates. Lastly, we discarded the medium and reloaded some fresh medium to obtain cell aggregates.

2.3.3. Cell seeding on 3D-printed hydrogel

Two different scaffolds ($\Phi = 4$ mm, $H = 2$ mm) with specific inner-structures (through hole was abbreviated as TH, and staggered hole was abbreviated as SH) seeded with cell suspension (CS) were named as CS/TH and CS/SH, and those seeded with cell aggregates (CA) were

named as CA/TH and CA/SH. After cell counting, an equal number of cells were seeded on scaffolds, the plates were incubated at 37 °C, 5% CO_2, and 95% humidity, and culture medium was added.

2.3.4. Evaluation of cell seeding efficiency

Live/dead staining was carried out to observe the distribution of cells on different groups (CS/TH, CS/SH, CA/TH, and CA/SH) one day after the cells were seeded. The cell morphology was observed using SEM, and cell number was evaluated using the *CCK-8* assay.

2.4. In vitro chondrogenic differentiation

To evaluate chondrogenic differentiation, hADSCs were seeded on the EM-SF_5GT_{15} SH scaffolds through CS or CA cell seeding method and cultured in the chondrogenic differentiation medium (HUXDM-9004, Cyagen, Suzhou, China), which contained dexamethasone, ascorbate, ITS, sodium pyruvate, proline, and TGF-β3. All samples were supplied with fresh culture medium every 3 d.

2.4.1. Histological and immunohistochemical analysis

After 14 and 28 d, samples were fixed with 4% paraformaldehyde, embedded in paraffin, and cut into 5-μm sections. Sections were stained with hematoxylin and eosin (H&E) for general histology, and Alcian blue and Safranin O staining were performed to evaluate chondrogenesis. Expressions of type II collagen (COL II), type I collagen (COL I), and aggrecan were examined by immunohistochemical staining. Paraffin-embedded sections were deparaffinized and dehydrated. Primary antibodies were incubated overnight in 4 °C. The SABC immunohistochemical kit (SA1020, Boster, Wuhan, China) was used and *DAB* (AR1022, Boster, Wuhan, China) was used as the chromonogen. Stained sections were scanned using a digital pathological scanning system (Aperio CS2, Leica, Germany) at 200 magnification.

2.4.2. Real-time polymerase chain reaction (RT-PCR)

RT-PCR, a method of quantitative PCR, was carried out to further evaluate the gene expression of chondrogenic differentiation. Briefly, total RNA was extracted and purified from the cells by using an RNA Extraction Kit (Solarbio), and the cDNA was synthesized using an all-in-one miRNA qPCR kit (GeneCopoeia, USA) according to the manufacturer's instructions. The amplification and gene expression of COL I, COL II, and aggrecan were carried out and evaluated with real-time qPCR (Quantstudio 6 flex, Life Technologies, USA) according to the manufacturer's instructions. With the $2^{-\Delta\Delta CT}$ method, we studied gene expression data. The primer sequences of each gene were shown in Supplementary Table 1.

2.5. In vivo evaluation of cartilage defect repair by 3D-printed hydrogel

2.5.1. Surgical procedure

All animal procedures were performed following the Guidelines for Care and Use of Laboratory Animals of Guangdong Pharmaceutical University and approved by the Animal Ethics Committee at Guangdong Pharmaceutical University. The experiments were performed on 12 New Zealand rabbits (male, 2.8–3.2 kg). In brief, after being anesthetized with 3% pentobarbital, rabbits were shaved and disinfected. The medial parapatellar approach was applied to expose the knee joints. The joints were fully exposed to develop a cylindrical osteochondral defect (4 mm diameter and depth) by a dental drill on both limbs at the center of the groove. After 2 days of routine culture, scaffolds with or without rabbit bone mesenchymal stem cell (BMSC, (RBXMX-01001, Cyagen, Suzhou, China)) aggregates were implanted into the defect, and the no-treatment defect was regarded as the control. On weeks 12 and 16, rabbits were euthanized by 3% pentobarbital overdose, and the femurs of the rabbits were sampled.

2.5.2. Histological and immunohistochemical analysis

For histological analysis, the samples were fixed in 4% paraformaldehyde for 3 d, followed by decalcification in 15% EDTA solution. Decalcification liquid was replaced daily until the sample could be embedded in paraffin. The center of the repair site was sliced into 5-μm sections followed by H&E staining, safranin-O/fast green staining, toluidine blue staining, as well as COL I and COL II immunohistochemical staining.

2.6. Statistical analysis

All measurements were expressed as the mean ± standard deviation. The *in vitro* experiments were repeated at least three times. Unpaired *t*-tests were used for comparison between two groups, and one-way ANOVA with Tukey's post-hoc test was used for comparison between two groups. A value of $P < 0.05$ was considered statistically significant. The analyses were performed using SPSS 25.0 software (SPSS, USA).

3. Results and discussion

For hyaline cartilage defects repair and long-term restoration, it is crucial to select an appropriate 3D scaffold with superior mechanical strength, suitable biocompatibility and degradation rate, and tailorable pore size and pore geometry [47–49]. In this study, SF and GT were combined as a pregel solution. Taking advantage of gelatin's thermosensitivity, fast gelation was achieved by controlling the platform temperature during the printing process. Moreover, the appropriate concentrations of HRP (60 units/mL) and H_2O_2 (5 mM) were selected to ensure the crosslinking process was mild and nontoxic [50,51]. Final stabilization of the printed structure was achieved by covalently crosslinking between the phenol groups on GT molecules and the amino acid residues on SF molecules under catalysis by the HRP/H_2O_2 system (Scheme 1).

3.1. Preparation and characterization of 3D-printed hydrogel

3.1.1. Morphology of the hydrogel

First, gelatin-tyramine was successfully synthesized. The chemical modification diagram is shown in Fig. S1(a), which could be proved by the H NMR results, as shown in Fig. S1(b). There were two new peaks at 6.72 ppm and 7.01 ppm in the modified gelatin, representing two proton absorption peaks on tyramine, which indicated the successful modification of tyramine. To determine suitable blending ratios of SF and GT, three types of thermoresponsive printing slurries were developed by varying the ratio of SF (w/v) with constant 15% (w/v) GT. All three groups had good printability based on the rheological characteristics (Fig. S1(c–e)). The SF-GT ink displayed thermoresponsive behavior before crosslinking, exhibiting liquid phase at physiological temperature (37 °C) and then transforming into a gel at temperatures below 25–30 °C. The SF-GT ink could be plotted using 200 μm needles, and there was no significant change in width among the three ink types. SF-GT could be plotted in 0°/90° layer patterns, resulting in rectangular macropores between the strands. Moreover, there was no collapse between layers within different printing orientations in different groups. In order to assess the morphology of the hydrogel scaffold, 3D microscope and SEM investigation were performed. The front and cross section views showed that all lyophilized scaffolds (E-SF_0GT_{15}, E-$SF_{2.5}GT_{15}$, E-SF_5GT_{15}, EM-$SF_{2.5}GT_{15}$, and EM-SF_5GT_{15}) had regularly arranged internally connected pores. The surface morphology of the fiber differed among the five groups (Fig. 1). In particular, the surface of the filament had obvious holes and folds only in the enzymatically crosslinked E-$SF_{2.5}GT_{15}$ group; in the EM-SF_5GT_{15} group, the surface of the filament was smooth and dense, which likely resulted from the configuration transition of SF due to treatment with methanol solution.

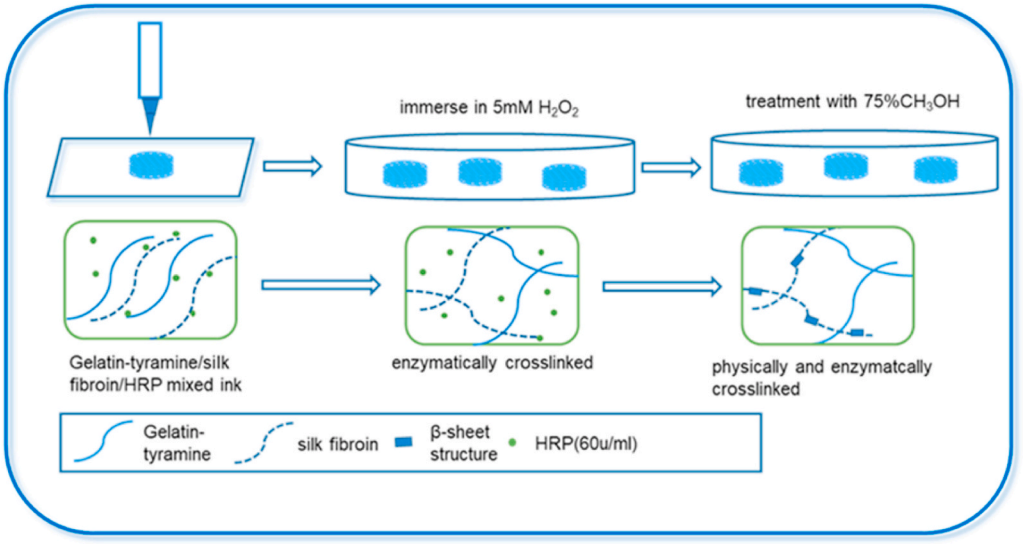

Scheme 1. Schematic diagrams of the 3D SF-GT hydrogel scaffold synthesis.

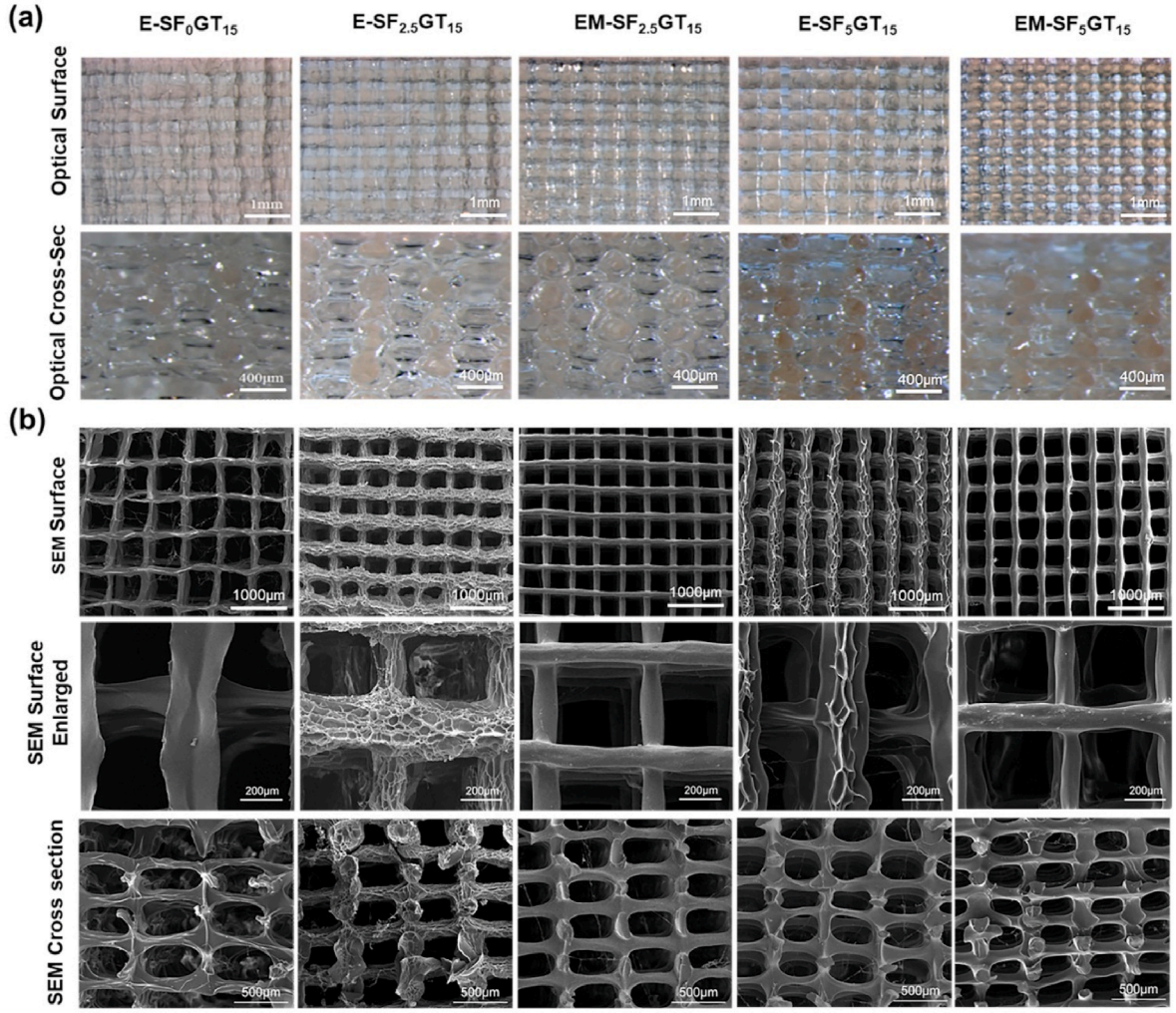

Fig. 1. (a) Optical images of surface and cross section of the SF-GT macro-porous hydrogel scaffolds made by 3D printing. (b) SEM images of surface and cross-sections of the SF-GT macro-porous hydrogel scaffolds.

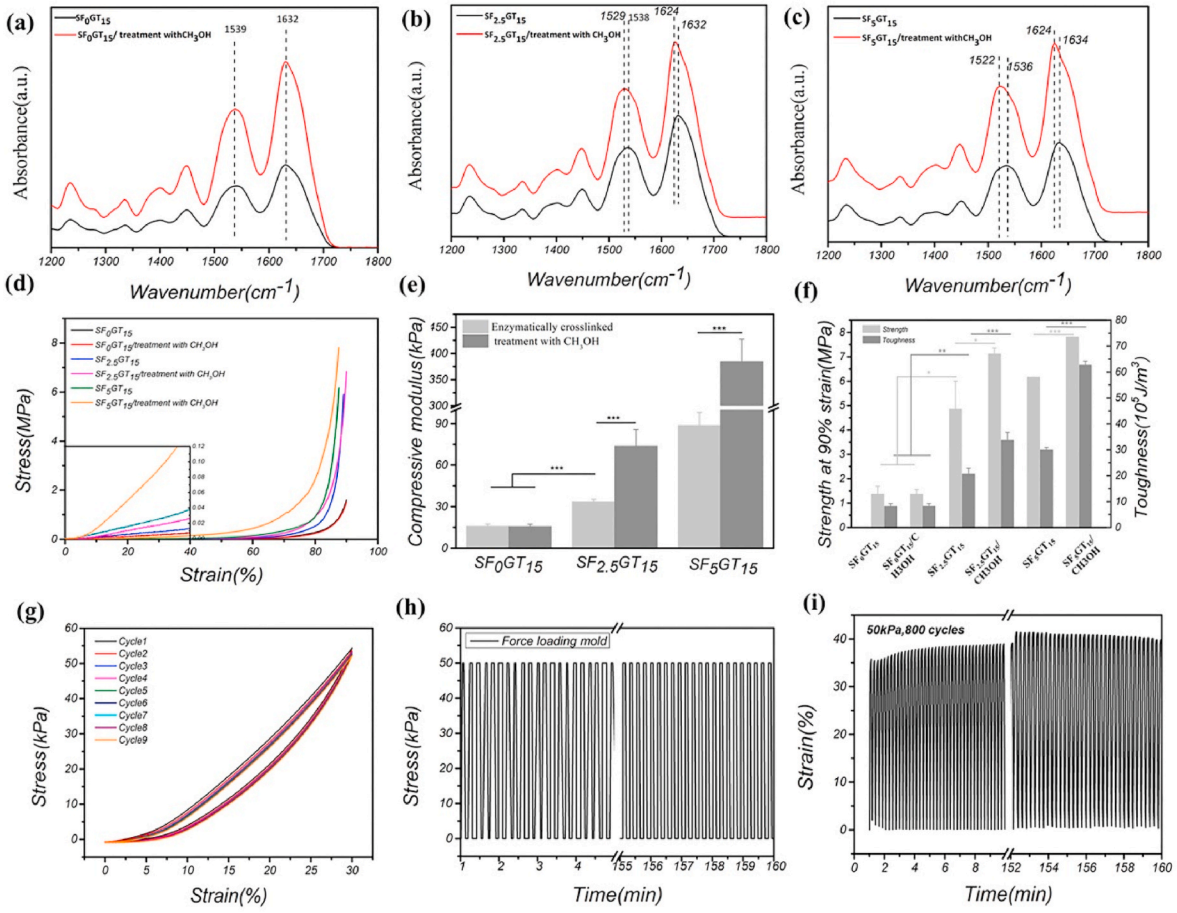

Fig. 2. FTIR spectrum of different 3D printed hydrogel scaffolds: (a) SF_0GT_{15} group; (b) $SF_{2.5}GT_{15}$ group; (c) SF_5GT_{15} group. Compressive mechanical performance of 3D printed hydrogel scaffolds: (d) stress-stain curves; (e) histogram of compressive modulus; (f) broken strength and toughness at 90% strain. The anti-fatigue property of scaffold "EM-SF_5GT_{15}": (g) the stress-strain curve under liner cyclic loading; (h) the loading force was kept at 50 kPa; (i) the change of strain undergoing 800 loading cycles. **p < 0.01; ***p < 0.001.

3.1.2. *The molecular structure of SF in the SF-GT hydrogel*

In order to further analyze and verify the conformation of silk fibroin molecules in hydrogel, infrared measurement was carried out. Fig. 2 (a–c) shows that the positions of absorption peaks in amide I (1600–1700 cm^{-1}) and amide II (1500–1600 cm^{-1}) did not change after methanol treatment in SF_0GT_{15} scaffolds; in contrast, in the $SF_{2.5}GT_{15}$ and SF_5GT_{15} groups, the absorption peaks shifted to low wavenumbers, and this effect became more obvious with the increase of SF content after being treated with methanol solution. According to previous reports, after the β-sheet conformational transformation of SF, the infrared absorption peaks of amide I and II regions shift to low wavenumber segments [32]. Therefore, in the SF-GT hydrogel with enzyme crosslinking, the conformation of SF was mainly random coil. In comparison, after the E–SF–GT hydrogel was treated with methanol, the conformation of silk fibroin was mainly β-sheet.

3.1.3. *Mechanical properties of the hydrogel*

The mechanical properties of 3D-printed SF-GT hydrogels were analyzed. As the concentration of SF increased, the compression moduli of hydrogels increased. Moreover, further enhancement of compression modulus was observed after treatment with methanol (Fig. 2(d) and (e)). Among them, the compression modulus of the SF_0GT_{15} scaffold with zero SF content did not change, staying at about 16 kPa; the compression modulus of the $SF_{2.5}GT_{15}$ scaffold increased from 33.5 ± 1.7 kPa to 73.9 ± 11.8 kPa; and the compression modulus of the SF_5GT_{15} scaffold increased from 88.7 ± 9.4 kPa to 384 ± 43.0 kPa. It was found that no SF-GT hydrogels were destroyed, and even their shape variables reached 90% (Fig. 2(f)).

The compression of cartilage *in vivo* is often repeated and dynamic, which requires the scaffold to have specific fatigue resistance. When a tissue engineering cartilage fills the defect, it will be affected by complex external forces from the subchondral bone and contralateral healthy cartilage in the joint, demanding excellent mechanical properties of the hydrogel scaffold [52]. Fig. 2(g) shows the stress–strain curve of the EM-SF_5GT_{15} hydrogel scaffold under the linear cyclic loading mode. After nine cycles, the curve of the hydrogel had a high degree of coincidence with the initial cycle. Moreover, the hysteresis loop formed by each cycle was small, which illustrates that the hydrogels had good recoverability. Fig. 2(h)–(i) shows that after 800 cycles of loading and unloading, the EM-SF_5GT_{15} hydrogel scaffold was able to return to its initial state before loading, and the resilience was close to 100%. Porous hydrogel scaffolds can be built through 3D printing in the manner of layer-by-layer accumulation and then adhered together. Compared to dense bulk hydrogels, the existence of pores conferred stronger deformability to the 3D printed hydrogels under the same external force, which helped hydrogels stay intact and gradually recover their shape. Therefore, after 800 cycles of the compression test, the morphology of the samples was not damaged. In brief, the 3D-printed EM-SF_5GT_{15} hydrogel scaffold has good compressive and fatigue resistance characteristics, so it can play a supporting role for tissue engineering cartilage.

3.1.4. *Analysis of swelling ratio, porosity, and degradation*

Fig. 3(a) and (b) show the swelling ratios of different 3D-printed SF-GT hydrogel scaffolds. Compared with the E-SF_0GT_{15} hydrogel, the

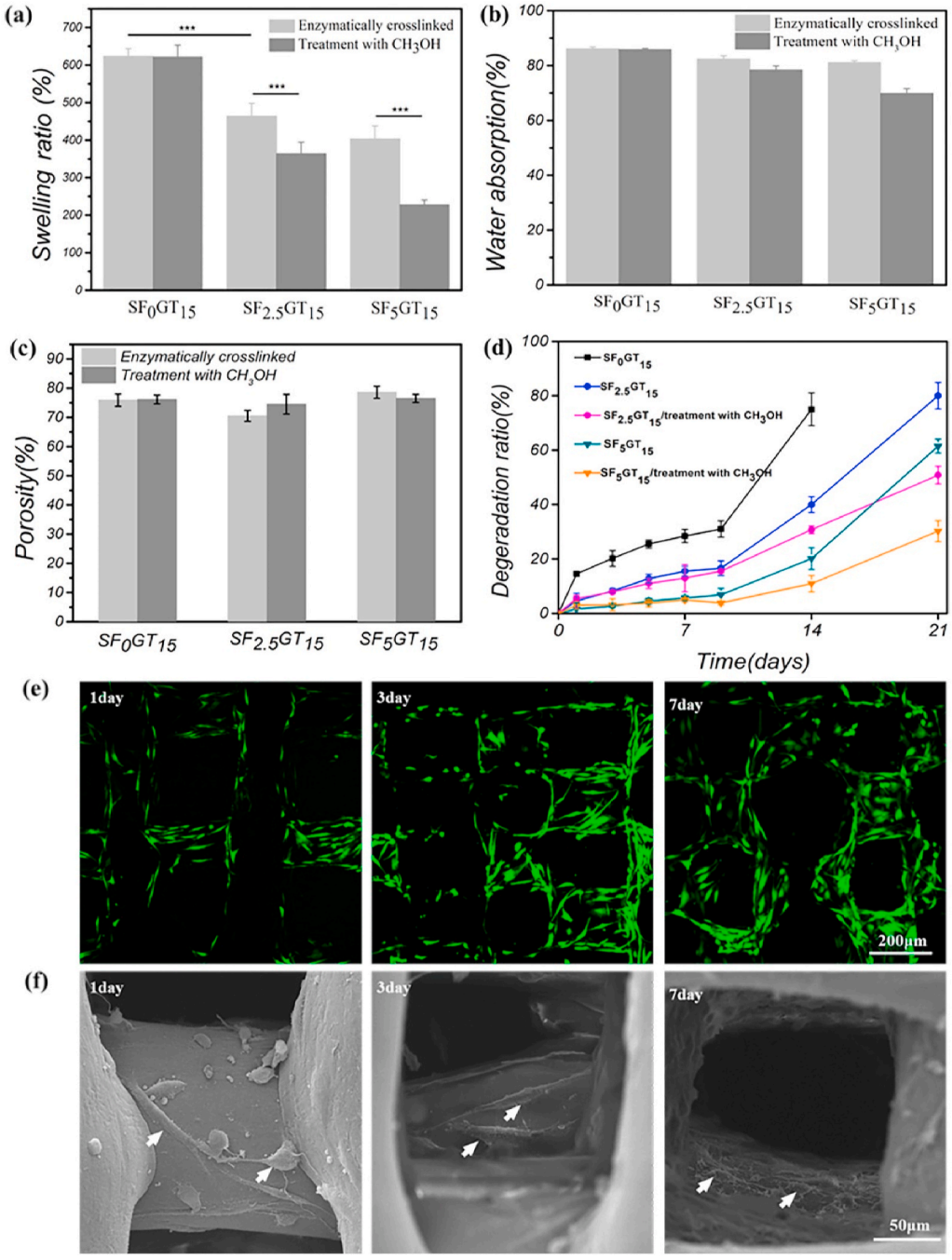

Fig. 3. (a) Swelling ratio, (b) water absorption, (c) porosity and (d) degradation of 3D printed hydrogel scaffolds. (e) Live/dead staining of cells on EM-SF_5GT_{15} scaffold, (f) SEM images of cells on EM-SF_5GT_{15} scaffold, the white arrow indicates the cell.

swelling ratio of hydrogel scaffolds decreased from 600% to about 400% after adding 2.5% or 5% SF. However, after further methanol treatment, the swelling ratio of hydrogel was significantly reduced to 200% in the EM-SF_5GT_{15} group. Because of the conformation transition of SF, the hydrophobicity of SF molecules, and the increase of gel crosslinking density, the swelling ratio of scaffolds decreased. Fig. 3(c) shows the porosity of different 3D-printed SF-GT hydrogel scaffolds. The porosity of these hydrogel scaffolds was maintained at about 70–75% due to the high repeatability of 3D printing. A limitation of gelatin is that it degrades too quickly to match the cartilage regeneration rate. Here, we showed that SF changed the degradation of 3D-printed SF-GT hydrogels. Specifically, increasing the SF content delayed the degradation of hydrogel scaffolds. As shown in Fig. 3(d), less than 20% of the initial mass of the E-SF_0GT_{15} hydrogel scaffolds remained at day 14, and the scaffold collapsed at day 21. In contrast, the E-$SF_{2.5}GT_{15}$ and E-SF_5GT_{15} scaffolds maintained around 60% and 80% of their original weights at day 14, and 30% and 40% at day 21. A similar trend was also recorded after the methanol treatment of hydrogel scaffolds. EM-$SF_{2.5}GT_{15}$ and EM-SF_5G_{15} maintained approximately 50% and 70% of their original weights at day 21. It is well known that a long time is needed to regenerate and repair cartilage, so the scaffold material should also have a long degradation time to match the rate of cartilage regeneration.

3.1.5. *Biocompatibility of hydrogels*

In order to verify the biocompatibility of hydrogels, cells on the scaffolds were observed by live/dead staining. As shown in Fig. 3(e),

there were no dead cells (stained in rad are dead) on the EM-SF_5GT_{15} scaffold during the culture time of 7 days, and the number of cells increased significantly with the increase of culture time. Fig. 3(f) shows the SEM results: after 1 d of inoculation, the cells had stretched out pseudopods to adhere to the scaffold; after 3 d, the cells were more spread out, adhered to the scaffold as fusiform, and had begun to grow inside the scaffold; after 7 d, through the electron microscope pictures with depth of field effect, we found that the cells grew on the filaments in the scaffold and were more spread, and many extracellular matrices were secreted around the filaments. The CCK-8 method was used to evaluate the proliferative ability of hADSCs inoculated on scaffolds. No difference in the number of proliferating cells was observed. Overall, 3D-printed SF-GT hydrogel scaffolds display good biocompatibility and enable cell proliferation.

3.2. *Different porous structures of hydrogels and cell seeding strategies*

In this study we developed two kinds of scaffolds with through holes (TH) or staggered holes (SH), and two kinds of cell seeding methods denoted as cell suspension (CS) and cell aggregate (CA). For cartilage tissue engineering, the optimum combination of cell seeding and scaffold was studied.

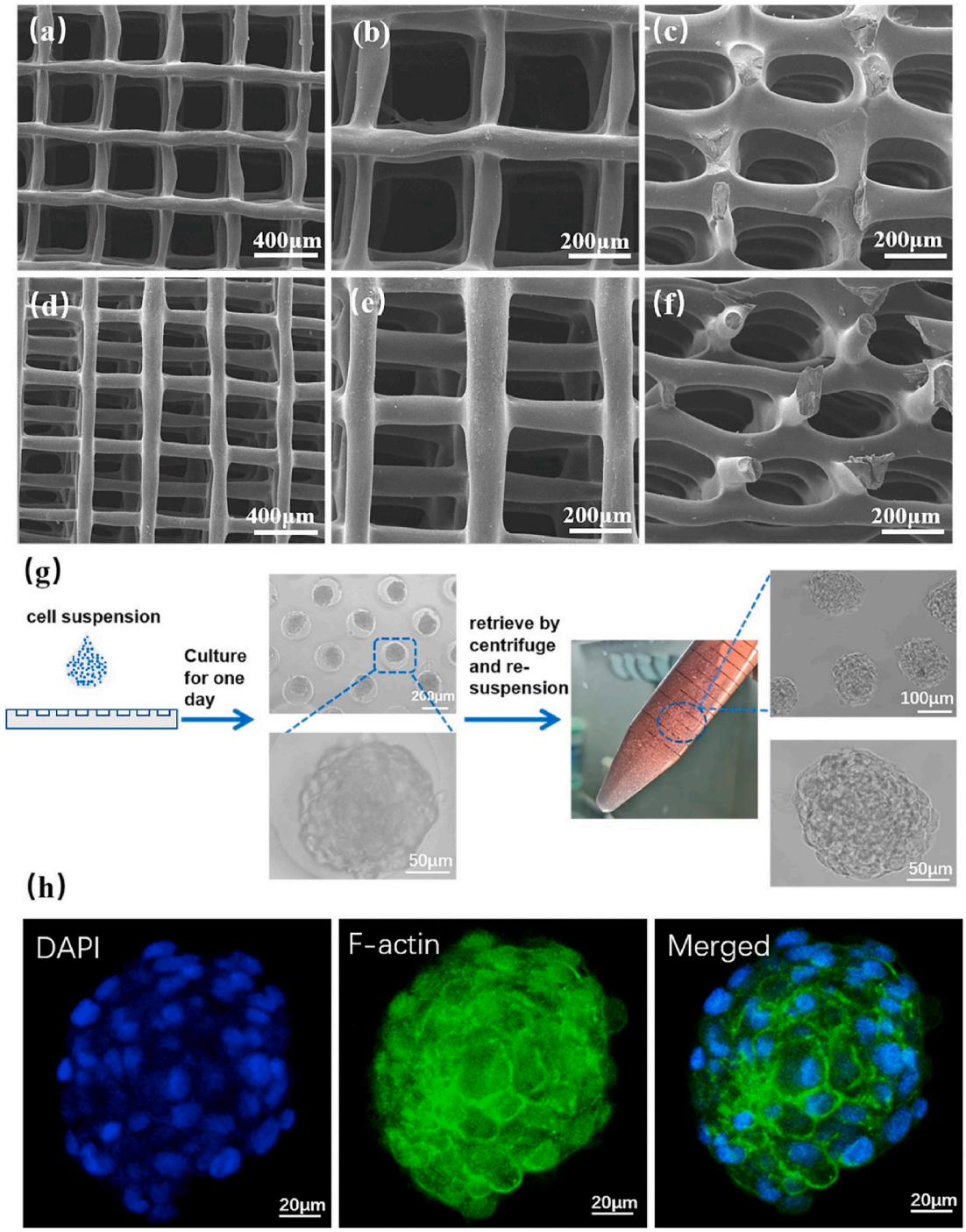

Fig. 4. SEM images of 3D printed EM-SF_5GT_{15} hydrogel scaffolds with different inner structure: through holes (TH) (a–b) top view, (c) side view; staggered holes (SH) (d–e) top view, (f) side view. (g) Preparation and collecting process of cell aggregates (CA). (h) Morphology of cells in a cell aggregate detect by F-actin immunofluorescence and DAPI for cell nuclei.

3.2.1. Through hole and staggered holes scaffolds

In order to improve the efficiency of cell inoculation, we designed a scaffold with a porous structure by changing the spatial position of the filament during the printing process. Frontal and lateral magnified images validated that the porous structure was prepared successfully. The through-hole scaffold internal structures were straight (Fig. 4(a–c)). Although the staggered-hole scaffold showed connected pores, and the vertical holes were misplaced (Fig. 4(d–f)). The internal structure of the scaffolds in the wet state was also scanned by micro-CT, and the results are shown in Fig. S3(a_1–a_3, b_1–b_3). The vertical section indicates that there were significant differences between the through hole and the staggered hole. There was no significant difference in porosity between the two kinds of scaffolds. Both porosities were about 75% (Fig. S3(c)). The results of the linear cyclic compression test are shown in Fig. S3(d). The stress–strain curves of the two kinds of scaffolds were relatively coincident. Therefore, this novel 3D-printed SF-GT hydrogel can not only mimic the mechanical properties of cartilage but also provide a customizable pore structure in order to optimize the nutrient- and gas-exchange of cells.

3.2.2. Cell aggregates

In order to obtain cell aggregates, we prepared a microwell array by agarose hydrogel. Agarose does not have cell adhesiveness, so cells will slide into the micropores of agarose under the action of gravity and then spontaneously form aggregates. The methods described in references were use, with some modifications [53,54]. The pattern on the mask was designed as a circular hole array with diameter of 200 μM, depth of 100 μM and spacing of 100 μM. To explore how many cells should be added to each pore in the process of cell aggregate preparation, we tested three gradient concentrations: 1×10^6, 2×10^6, and 4×10^6 cells/mL. We found that the cell seeding concentrations of 1×10^6 and 4×10^6 cells/mL were respectively too low and too high, resulting in the uneven size of the cell aggregates or the connection of cells over a large area. However, with the concentration of 2×10^6 cells/mL, the cells were able to form a uniform aggregate with a diameter of about 150 μm (Fig. S4). Cell aggregates maintained a uniform round shape during the process of being collected by centrifugation and resuspended in fresh culture medium (Fig. 4(g)). Cytoskeleton staining results further displayed that many cells in a cell aggregate presented uniform round cell morphology (Fig. 4(h)).

3.2.3. Cellular inoculation efficiency

When cell suspension seeding was used, the cells could be seeded on both scaffolds, but more cells adhered to the staggered-hole scaffold (Fig. 5(a)). When cell aggregate seeding was used, it was difficult for cell aggregates to adhere to the through hole scaffold, and more cell aggregates adhered to the staggered-hole scaffold (Fig. 5(a)). Importantly, the cell location and its relationship with scaffold fiber was different in staggered-hole scaffolds. For cell suspension seeding, from the SEM results of days 1, 3, and 7, we found cells first adhered to the fiber and then spread around it; indeed, few cells were in the holes. On the contrary, cell aggregates filled the holes initially, and only a small number of cells spread and adhered to fiber (Fig. 5(b)). Furthermore, cell numbers on different groups of scaffolds 1 d after inoculation were measured by CCK-8 (Fig. S5), collectively indicating that the discrepancies resulted from different combinations. Although the CS/SH was superior to the CS/TH, the CA/SH was best.

In general, cell therapy for cartilage regeneration often shows inefficient and inhomogeneous regeneration, so it is always confined to treat minimal local cartilage defects [55]. How to uniformly distribute high densities of cells within scaffolds has remained a persistent challenge for cartilage tissue engineering. The smooth surface and large pores of a scaffold usually cause unfavorable effects on cell residence and have an adverse effect on the attachment of many cellular and biological factors [14,56]. As shown in Fig. 5(b), there were few cells in the pore space. However, the pores were filled in the CA/SH group. Previous investigation of 3D fabricated porous scaffolds also showed that cell suspension could not seed a sufficiently large number of cells into the construct. As a result, the quality of the regenerated tissue matrix was affected by the distribution and organization of cells [57]. Based on these results, cell aggregate seeding could enable efficient cell penetration into the scaffold to obtain the spatial distribution of cells throughout the construct, leading to a high-quality matrix organization.

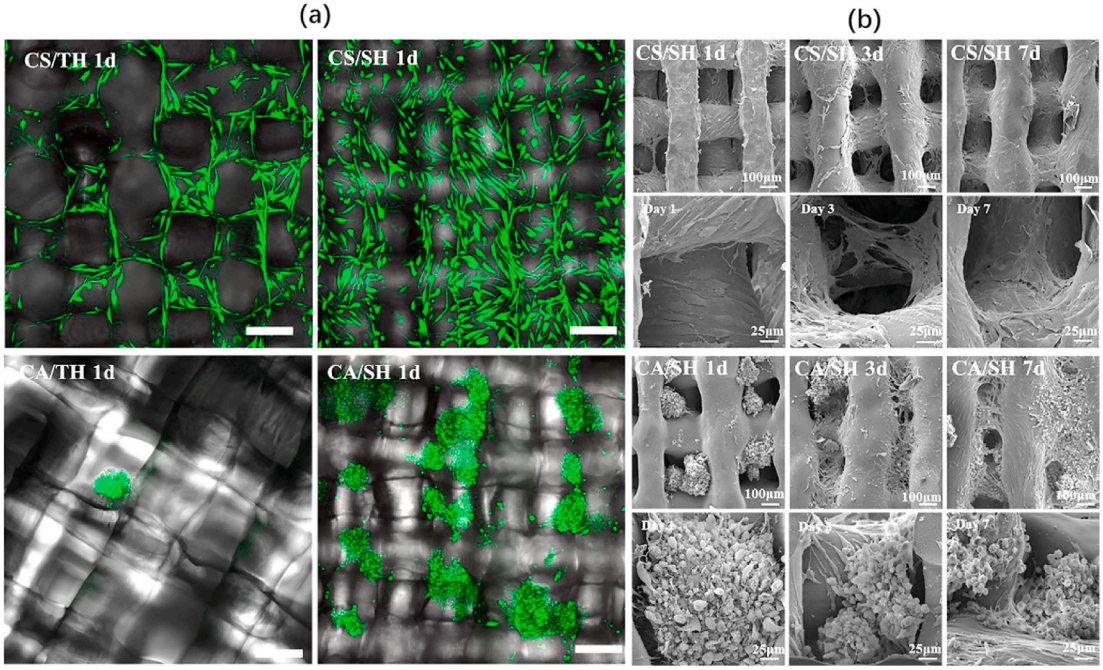

Fig. 5. (a) Live/dead staining result (green, red and bright filed merged) of CS/TH, CS/SH, CA/TH and CA/SH at 1 day, where green fluorescence indicates live cells and red fluorescence indicates dead cells. Scale bar = 200 μm. (b) SEM of CS/SH and CA/SH at 1, 3 and 7 days. (For interpretation of the references to colour in this figure legend, the reader is referred to the Web version of this article.)

3.3. Tissue engineering cartilage formed by CS or CA on the staggered-hole scaffold

With the knowledge that staggered holes improve cell seeding efficiency, we seeded cell suspensions and cell aggregates on the scaffold with staggered holes. Both were cultured with the chondrogenic medium for fabrication tissue engineering cartilage (The scaffold and tissue engineering cartilage pictures are available in Fig. S6). The cells and matrices secreted by the cells were studied by H&E (demonstration of primary findings based on the nucleus and cytoplasmic morphological change), Safranin O staining (glycosaminoglycan distribution), and Alcian blue (sulfated proteoglycan distribution) staining (Fig. 6). In the results of H&E staining, compared with the CS/SH group, the CA/SH group had higher cell density at 14 d and 28 d, and the pores of CA/SH scaffolds were filled with many more cells and matrices. Safranin O and Alcian blue staining results were more in-depth with the increase of time, indicating the increase of extracellular matrix secretion. Preliminary histological examination showed that with the extension of *in vitro* culture time, both cell-laden constructs gradually displayed cartilage features. In order to demonstrate the effects of different cell seeding methods on the types of newly formed cartilage, we examined the expression of type I collagen (COL I), type II collagen (COL II), and aggrecan by immunohistochemistry (Fig. 6). The expression level of COL I (a high proportion of collagen in fibrocartilage) was higher in the CS/SH group than the CA/SH group at 14 d and 28 d. In contrast, the expression level of COL II was higher in the CA/SH group than the CS/SH group. Furthermore, the aggrecan expression had no noticeable difference among groups at the same time point. RT-qPCR was performed to evaluate gene expression levels of SOX-9, Aggrecan, COL I, and COL II, and results are shown in Fig. 7. The expressions of SOX-9 and Aggrecan genes in the CA/SH and CS/SH groups at 14 d and 28 d were higher than the control, but there were no differences between the two groups at the same time points. The expressions of COL I and COL II genes had a significant difference: the COL I expression was higher in the CS/SH group, whereas the COL II expression was higher in the CA/SH group, and the ratio of the expression COL I and COL II within each group at 14 d and 28 d had a significant difference. Cell aggregates favored the retention of transplanted cells into the holes of 3D-printed scaffolds because of their size and chance to contact the scaffold, which may be favorable for the extracellular matrix production of cartilage and chondrogenesis, thus improving cartilage tissue engineering.

Cells seeded on scaffolds or cultured in monolayers, microarrays, or pellets assume varied morphologies and secrete different signaling molecules [34,37]. Recently, 3D cellular aggregates, instead of 2D cell sheets, have been employed as building blocks in order to understand the principles of cell–cell and cell–matrix adhesion [58,59]. Cell aggregates can better simulate real cell morphology, fate, and metabolic activities *in vivo*. In our study, the cell morphology and matrix structure in cartilage tissue engineering were found to be closely related to the fabrication strategy, since distinct differences were observed between the cell aggregate seeding and cell suspension seeding methods. As shown in Fig. 6, cell aggregate seeding regulates a round, spherical shape, allowing stem cells to produce more type II collagen but less type I collagen to obtain a hyaline cartilage phenotype. Cell suspension seeding regulates a spreading fibroblast-like morphology, which makes stem cells produce more type I collagen but less type II collagen to obtain fibrocartilage. The most likely causes of the difference in chondrogenic differentiation are enhanced gap junction or N-cadherin mediated cell−cell communication and matrix production by the condensation phenomenon of MSCs [60,61]. However, there are a few contradictory studies that reported failure to redifferentiate or subsequent insufficient matrix synthesis by cellular aggregates when encapsulated in hydrogels. For instance, encapsulation of small aggregates of bovine chondrocytes in photopolymerizable hydrogels was found to inhibit the extracellular matrix production of clustered chondrocytes compared to dispersed chondrocytes [62]. Furthermore, aggregates failed to offer any beneficial effects over dispersed cells in alginate gel encapsulation with

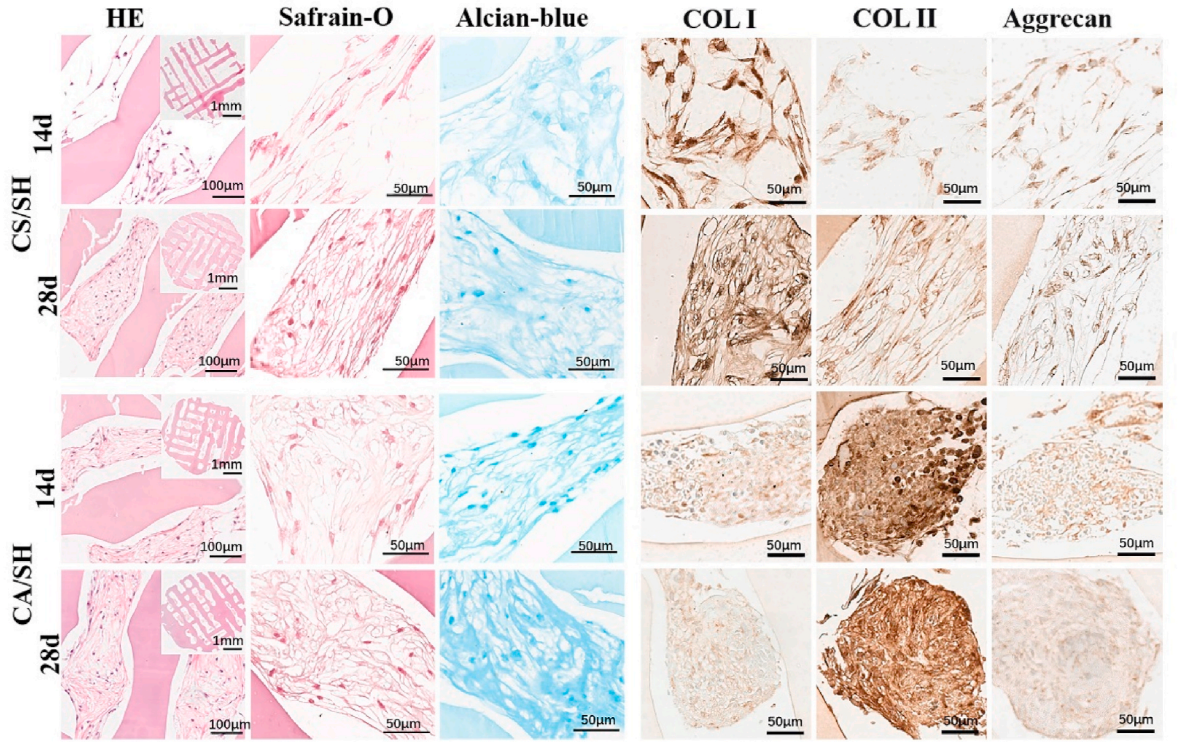

Fig. 6. Evaluation of cartilage formation of CA/SH and CS/SH cultured in chondrogenic differentiation medium. The sections were stained with H&E, safranine-o, alician-blue after 14 and 28 days of culture, also COL I, COL II and Aggrecan immunohistochemical staining. (For interpretation of the references to colour in this figure legend, the reader is referred to the Web version of this article.)

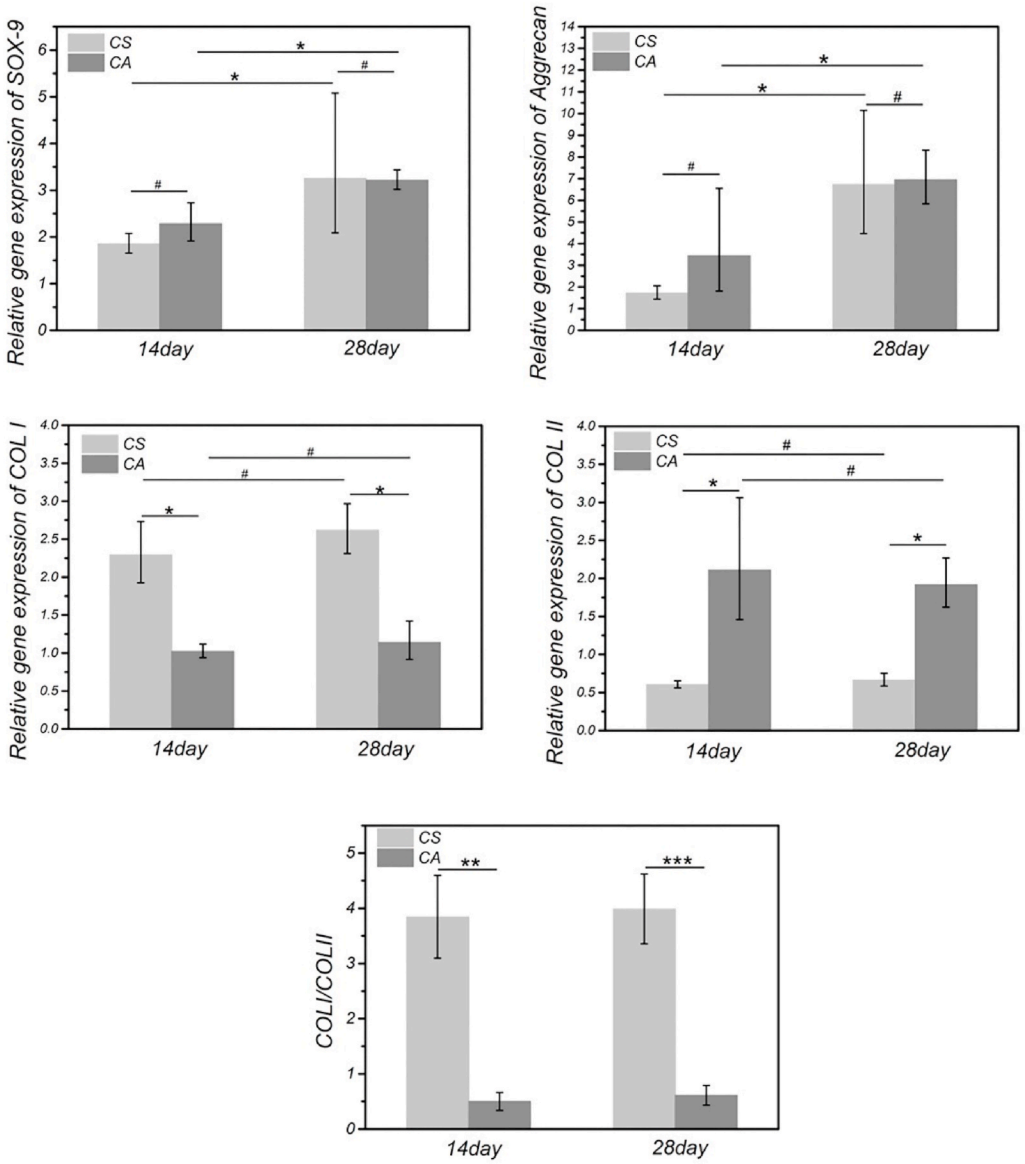

Fig. 7. Chondrogenic differentiation of CS and CA on 3D printed EM-SF_5GT_{15} hydrogel scaffolds with staggered holes. Chondrogenic relative gene (SOX-9, Aggrecan, COL I, COL II) expression were analyzed by qRT-PCR. **p < 0.01; ***p < 0.001.

subsequent downregulation in the resultant chondrogenic marker gene expression for the macroaggregates culture [63]. We speculate that the primary reason may be cells in scaffolds adhere to concrete surfaces differently from cells embedded in a hydrogel matrix. Further experimental investigations are needed to estimate MSC chondrogenesis in different environments.

3.4. *In vivo study*

A significant limitation of cartilage tissue engineering is the lack of understanding of how to distinguish the development of neo-cartilage construct regarding phenotypically stable articular cartilage and transient cartilage. The ability of staggered-hole EM-SF_5GT_{15} scaffolds with or without cell aggregate seeding to repair rabbit articular cartilage defects was evaluated (images of the implantation procedure were in Fig. S7). Twelve weeks after surgery, the cartilage defects in all groups displayed a distinct boundary between the defect area and the surrounding normal tissue (Fig. 8). Particularly, the defect was irregular in the non-treated group, and the defect area was filled with fibrous-like tissue. The defects in the scaffold group and scaffold with CA group appeared similar macroscopically, that is, they were partly covered with cartilage-like tissues. Comparing the center of the defect area, we can see that in the scaffold group there was little tissue, but in the scaffold with CA group, more tissue was regenerated, leaving only a small crevice. Sixteen weeks after surgery, the defects in three groups were filled (Fig. 8), but only the scaffold with CA group showed a smooth articular surface. There was a large amount of fibrous tissue in the control group, and the center of the defect in the scaffold group was slightly depressed.

The histological results (Fig. 9) showed microscopic images of paraffin-embedded tissue sections. According to the results of H&E staining at 12 weeks and 16 weeks, the cartilaginous tissue in the defect area was different among the three groups. While primarily fibrous scar tissue formation was observed in the control group, more cartilage-like tissue was observed in the scaffold group. However, the cell distribution was disorderly, and more significant cartilage tissue regeneration was observed in the scaffold with CA group. GAG distribution of the new cartilage tissue and the subchondral bone regeneration were analyzed by safranin-O/fast green staining. As shown in Fig. 9, safranin-O results showed that there was less newly formed cartilage in control and scaffold group at 12 weeks, but a substantial amount newly cartilage in the

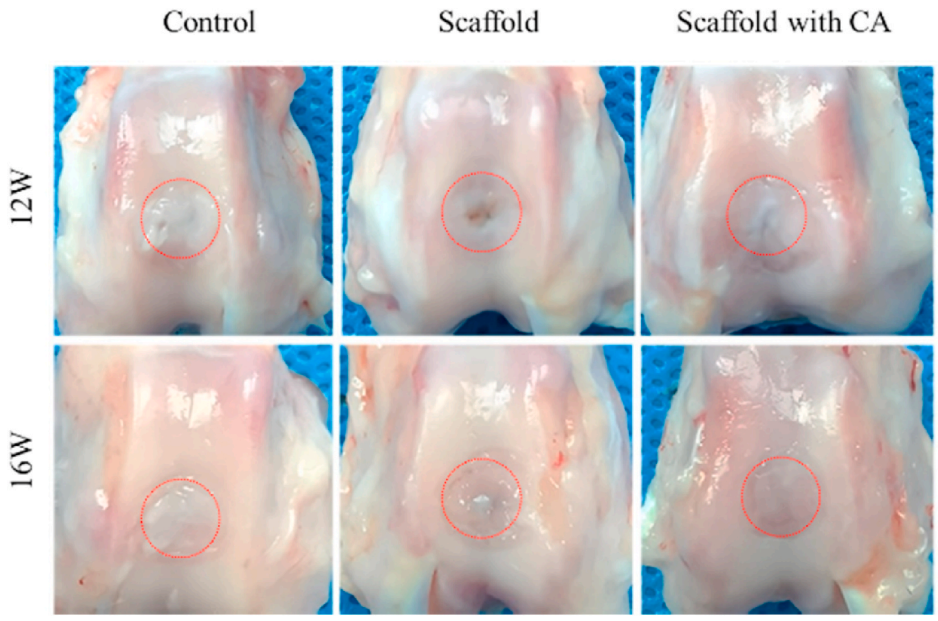

Fig. 8. *In vivo* animal tests. Harvested joints after 12 weeks and 16 weeks showing regenerated cartilage tissue.

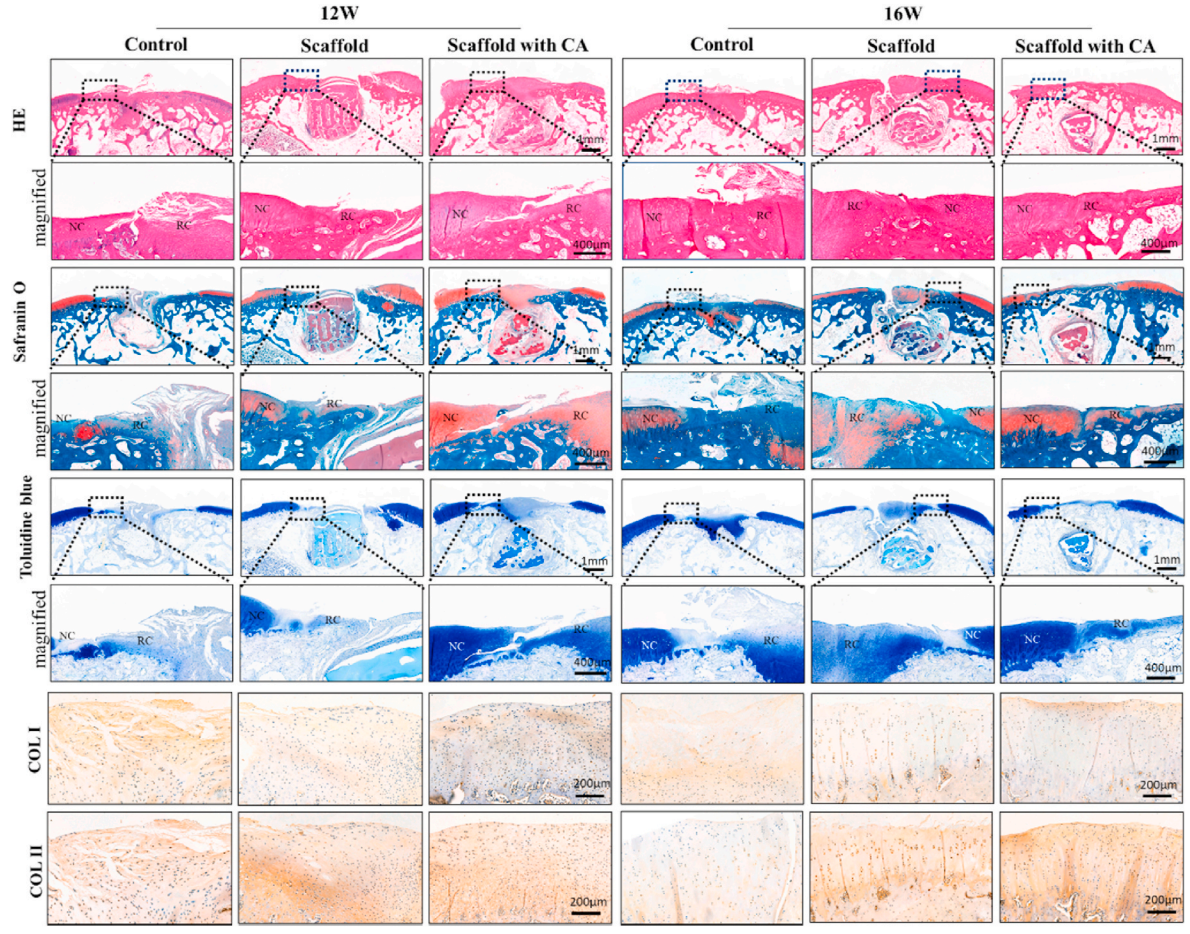

Fig. 9. Histological assessment of regenerated cartilage *in vivo*. H&E, safranin O/fast green and toluidine blue staining of repaired cartilage and 12 and 16 weeks. Immunohistochemical staining for COL I and COL II at 12 and 16 weeks. (NC: normal cartilage, RC: regenerated cartilage). (For interpretation of the references to colour in this figure legend, the reader is referred to the Web version of this article.)

center of the defect in scaffold with CA group. After 16 weeks, a well-arranged cartilage layer was formed on the complete subchondral bone layer in scaffold with CA group, but there was only a disorderly chunk of newly cartilage in the center of control and scaffold group. Toluidine blue staining can show the presence of proteoglycans in cartilage because of its high affinity for the sulfate groups of proteoglycans. In detail, the newly cartilage layer fully recovered the consistency of the joint surface. Immunohistochemical analyses were carried out to show the expression of collagen at the defect center. At 16 weeks, the scaffold with CA produced more COL II enriched hyaline-like cartilage, with COL I mainly observed in the superficial zone. The scaffold group tended to generate hyaline-like cartilage but showed progressive thinning and rough surface. The control group showed defect filling with common fibrocartilage.

These magnified images of histological staining (HE, Safrain O and Toulidine blue) in Fig. 9, also revealed that the satisfactory regenerated cartilage structures, interface integration of cartilage and osteochondral interfaces in scaffold with CA group were better than other two groups. Immunohistochemistry staining of collagen II and collagen I in Fig. 9 indicated synthesis of collagens in the extracellular matrix and the cell distribution details. Among the control, scaffold and scaffold with CA groups, the content of stained Col II in the regenerated cartilage of scaffold with CA group increased significantly after 16 weeks treatment. There was some cartilage-like tissue at 12 weeks in control and scaffold group, but the chondrocyte-like cell in these two groups were observed to have an irregular distribution with treatment time extension at 16 weeks. There was a cartilage layer in scaffold with CA group, with implant time increased the cell distribution tended to be normal These results together demonstrate that the EM-SF_5GT_{15} scaffold with cell aggregate seeding could effectively improve articular cartilage repair and regeneration.

As novel materials are developed for cartilage repair and regeneration, the regulatory requirements about physical three-dimensional structure must be considered [64]. In this study, the EM-SF_5GT_{15} scaffold with microporous structure enable sufficient transport of gases, nutrients, and bioactive molecules throughout the scaffold to allow new tissue maintain appropriate anabolic activities same as cartilage development. And the CA provides a cell differentiation guiding support and avoids a common consequent generation of fibrocartilaginous tissues. There has been a considerable progress in the 3D printing domain with various types of hydrogels being printed and tested as a cartilage tissue engineering scaffold. The most commonly use hydrogels including alginate, GelMA and collagen, but maintaining the shape fidelity and pore integrity with these hydrogels is difficult. Many synthetic polymers such as PCL [64,65] were coupled with the hydrogel to improve the structure fidelity. Articular cartilage is an inhomogeneous, anisotropic, poro-viscoleastic material and it shows changed compressive modulus from the joint surface to the deep zone of articular cartilage. The compressive aggregate modulus of joint articular cartilage ranges from 0.08 to 2 MPa, the compressive matrix modulus value of a mature rabbit articular cartilage about 0.8 Mpa, and 1.03 $\pm$ 0.48 MPa in human [66–69]. 3D-printed biohybrid gradient hydrogel scaffolds synthesized though N-acryloyl glycinamide, and N-[tris(hydroxymethyl)methyl] acrylamide copolymerization have compressive modulus level about 23–115 kPa can accelerate simultaneous regeneration of cartilage and subchondral bone in a rat model [70]. In this study we found the SF-GT scaffold with 384 $\pm$ 43.0 kPa played an important role during physiological loading, in favor of the newly cartilage staying in a stable mechanical environment.

4. Conclusions

This study developed an effective method for cartilage tissue engineering by combining a 3D-printed SF-GT hydrogel with stem cell aggregates. The internal structure of the scaffold was designed to improve the retention of cell aggregates in the scaffold. In the stage of differentiation, stem cells seeded on the scaffolds via cell suspension tended to present fibrochondrocyte phenotype, whereas cell aggregate seeding led to higher levels of synthetic COL II and showed hyaline cartilage phenotype. Specifically, *in vivo* studies on the performance of the scaffold combined with stem cells indicated that the 3D-printed EM-SF_5GT_{15} hydrogel with cell aggregates seeding method may have broad clinical applications in promoting cartilage repair.

Declaration of competing InterestCOI

The authors declare that they have no known competing financial interests or personal relationships that could have appeared to influence the work reported in this paper.

CRediT authorship contribution statement

Qingtao Li: Conceptualization, Investigation, Methodology, Project administration, Writing – original draft. **Sheng Xu:** Conceptualization, Investigation, Methodology, Project administration, Writing – original draft. **Qi Feng:** Data curation, Formal analysis, Investigation, Writing – review & editing. **Qiyuan Dai:** Methodology, Investigation, Software. **Longtao Yao:** Data curation, Methodology, Investigation. **Yichen Zhang:** Data curation, Methodology, Investigation. **Huichang Gao:** Resources, Methodology. **Hua Dong:** Resources, Methodology. **Dafu Chen:** Funding acquisition, Supervision, Writing – review & editing. **Xiaodong Cao:** Project administration, Funding acquisition, Supervision, Writing – review & editing.

Acknowledgment

This work was financially supported by the National Natural Science Foundation of China (Grant nos. 52073103, 51873069 and 51873071), the National Key R&D Program of China (Grant No. 2018YFC1106300), Beijing Municipal Health Commission (Grant nos. BMHC-2019-9, BMHC-2018-4 and PXM2020_026275_000002), the funds for Zhongshan Innovation Project of high-end Scientific Research Institutions (Grant No. 2020AG020).

Appendix A. Supplementary data

Supplementary data to this article can be found online at https://doi.org/10.1016/j.bioactmat.2021.03.013.

References

[1] Y. Krishnan, A.J. Grodzinsky, Cartilage diseases, Matrix Biol. 71–72 (2018) 51–69.
[2] M. Bhattacharjee, J. Coburn, M. Centola, S. Murab, A. Barbero, D.L. Kaplan, I. Martin, S. Ghosh, Tissue engineering strategies to study cartilage development, degeneration and regeneration, Adv. Drug Deliv. Rev. 84 (2015) 107–122.
[3] M. Farokhi, F. Mottaghitalab, Y. Fatahi, M.R. Saeb, P. Zarrintaj, S.C. Kundu, A. Khademhosseini, Silk fibroin scaffolds for common cartilage injuries: possibilities for future clinical applications, Eur. Polym. J. 115 (2019) 251–267.
[4] E.A. Makris, A.H. Gomoll, K.N. Malizos, J.C. Hu, K.A. Athanasiou, Repair and tissue engineering techniques for articular cartilage, Nat. Rev. Rheumatol. 11 (1) (2015) 21–34.
[5] K.L. Spiller, S.A. Maher, A.M. Lowman, Hydrogels for the repair of articular cartilage defects, Tissue Eng. B Rev. 17 (4) (2011) 281–299.
[6] M. Liu, X. Zeng, C. Ma, H. Yi, Z. Ali, X.B. Mou, S. Li, Y. Deng, N.Y. He, Injectable hydrogels for cartilage and bone tissue engineering, Bone Res 5 (2017) 20.
[7] J.W. Li, G.J. Chen, X.Q. Xu, P. Abdou, Q. Jiang, D.Q. Shi, Z. Gu, Advances of injectable hydrogel-based scaffolds for cartilage regeneration, Regen. Biomater. 6 (3) (2019) 129–140.
[8] L.-S. Wang, C. Du, W.S. Toh, A.C.A. Wan, S.J. Gao, M. Kurisawa, Modulation of chondrocyte functions and stiffness-dependent cartilage repair using an injectable enzymatically crosslinked hydrogel with tunable mechanical properties, Biomaterials 35 (7) (2014) 2207–2217.
[9] P.J. Martens, S.J. Bryant, K.S. Anseth, Tailoring the degradation of hydrogels formed from multivinyl poly(ethylene glycol) and poly(vinyl alcohol) macromers for cartilage tissue engineering, Biomacromolecules 4 (2) (2003) 283–292.
[10] S. Chu, M.M. Maples, S.J. Bryant, Cell encapsulation spatially alters crosslink density of poly(ethylene glycol) hydrogels formed from free-radical polymerizations, Acta Biomater. 109 (2020) 37–50.

[11] D.J. Griffon, M.R. Sedighi, D.V. Schaeffer, J.A. Eurell, A.L. Johnson, Chitosan scaffolds: interconnective pore size and cartilage engineering, Acta Biomater. 2 (3) (2006) 313–320.
[12] S.-M. Lien, L.-Y. Ko, T.-J. Huang, Effect of pore size on ECM secretion and cell growth in gelatin scaffold for articular cartilage tissue engineering, Acta Biomater. 5 (2) (2009) 670–679.
[13] C. Fan, D.-A. Wang, Macroporous hydrogel scaffolds for three-dimensional cell culture and tissue engineering, Tissue Eng. B Rev. 23 (5) (2017) 451–461.
[14] Q.Q. Yao, B. Wei, N. Liu, C.S. Li, Y. Guo, A.N. Shamie, J. Chen, C. Tang, C.Z. Jin, Y. Xu, X.W. Bian, X.L. Zhang, L.M. Wang, Chondrogenic regeneration using bone marrow clots and a porous polycaprolactone-hydroxyapatite scaffold by three-dimensional printing, Tissue Eng. 21 (7–8) (2015) 1388–1397.
[15] S. Reed, G. Lau, B. Delattre, D.D. Lopez, A.P. Tomsia, B.M. Wu, Macro- and micro-designed chitosan-alginate scaffold architecture by three-dimensional printing and directional freezing, Biofabrication 8 (1) (2016), 015003.
[16] G. O'Connell, J. Garcia, J. Amir, 3D bioprinting: new directions in articular cartilage tissue engineering, ACS Biomater. Sci. Eng. 3 (11) (2017) 2657–2668.
[17] P.L. Lewis, R.M. Green, R.N. Shah, 3D-printed gelatin scaffolds of differing pore geometry modulate hepatocyte function and gene expression, Acta Biomater. 69 (2018) 63–70.
[18] A.S. Caldwell, B.A. Aguado, K.S. Anseth, Designing microgels for cell culture and controlled assembly of tissue microenvironments, Adv. Funct. Mater. 30 (37) (2019) 1907670.
[19] Q. Feng, Q. Li, H. Wen, J. Chen, M. Liang, H. Huang, D. Lan, H. Dong, X. Cao, Injection and self-assembly of bioinspired stem cell-laden gelatin/hyaluronic acid hybrid microgels promote cartilage repair in vivo, Adv. Funct. Mater. 29 (50) (2019) 1906690.
[20] X. Nie, Y.J. Chuah, W. Zhu, P. He, Y. Peck, D.-A. Wang, Decellularized tissue engineered hyaline cartilage graft for articular cartilage repair, Biomaterials 235 (2020) 119821.
[21] C.M. Hwang, S. Sant, M. Masaeli, N.N. Kachouie, B. Zamanian, S.H. Lee, A. Khademhosseini, Fabrication of three-dimensional porous cell-laden hydrogel for tissue engineering, Biofabrication 2 (3) (2010) 12.
[22] G. Ying, N. Jiang, C. Yu, Y.S. Zhang, Three-dimensional bioprinting of gelatin methacryloyl (GelMA), Bio-Des. and Manuf. 1 (4) (2018) 215–224.
[23] J. Yin, M.L. Yan, Y.C. Wang, J.Z. Fu, H.R. Suo, 3D bioprinting of low-concentration cell-laden gelatin methacrylate (GelMA) bioinks with a two-step cross-linking strategy, Acs Appl. Mater. Inter. 10 (8) (2018) 6849–6857.
[24] N.C. Negrini, N. Celikkin, P. Tarsini, S. Fare, W. Swieszkowski, Three-dimensional printing of chemically crosslinked gelatin hydrogels for adipose tissue engineering, Biofabrication 12 (2) (2020) 16.
[25] L. Shao, Q. Gao, C. Xie, J. Fu, M. Xiang, Y. He, Synchronous 3D bioprinting of large-scale cell-laden constructs with nutrient networks, Advanced Healthc. Mater. 9 (15) (2019) 1901142.
[26] Y. Wang, D.J. Blasioli, H.-J. Kim, H.S. Kim, D.L. Kaplan, Cartilage tissue engineering with silk scaffolds and human articular chondrocytes, Biomaterials 27 (25) (2006) 4434–4442.
[27] Y.Z. Wang, U.J. Kim, D.J. Blasioli, H.J. Kim, D.L. Kaplan, In vitro cartilage tissue engineering with 3D porous aqueous-derived silk scaffolds and mesenchymal stem cells, Biomaterials 26 (34) (2005) 7082–7094.
[28] Y. Chen, T. Wu, S. Huang, C.-W.W. Suen, X. Cheng, J. Li, H. Hou, G. She, H. Zhang, H. Wang, X. Zheng, Z. Zha, Sustained release SDF-1 alpha/TGF-beta 1-loaded silk fibroin-porous gelatin scaffold promotes cartilage repair, Acs Appl. Mater. Inter. 11 (16) (2019) 14608–14618.
[29] N. Fazal, N. Latief, Bombyx mori derived scaffolds and their use in cartilage regeneration: a systematic review, Osteoarthritis Cartilage 26 (12) (2018) 1583–1594.
[30] Q.S. Wang, G.C. Han, S.Q. Yan, Q. Zhang, 3D printing of silk fibroin for biomedical applications, Materials 12 (3) (2019) 504.
[31] N.R. Raia, B.P. Partlow, M. McGill, E.P. Kimmerling, C.E. Ghezzi, D.L. Kaplan, Enzymatically crosslinked silk-hyaluronic acid hydrogels, Biomaterials 131 (2017) 58–67.
[32] O. Hasturk, K.E. Jordan, J. Choi, D.L. Kaplan, Enzymatically crosslinked silk and silk-gelatin hydrogels with tunable gelation kinetics, mechanical properties and bioactivity for cell culture and encapsulation, Biomaterials 232 (2020) 119720.
[33] S. Das, F. Pati, Y.-J. Choi, G. Rijal, J.-H. Shim, S.W. Kim, A.R. Ray, D.-W. Cho, S. Ghosh, Bioprintable, cell-laden silk fibroin-gelatin hydrogel supporting multilineage differentiation of stem cells for fabrication of three-dimensional tissue constructs, Acta Biomater. 11 (2015) 233–246.
[34] A. Nazempour, B.J. Van Wie, Chondrocytes, mesenchymal stem cells, and their combination in articular cartilage regenerative medicine, Ann. Biomed. Eng. 44 (5) (2016) 1325–1354.
[35] J. Chaumel, M. Schotte, J.J. Bizzarro, P. Zaslansky, P. Fratzl, D. Baum, M.N. Dean, Co-aligned chondrocytes: zonal morphological variation and structured arrangement of cell lacunae in tessellated cartilage, Bone 134 (2020) 13.
[36] T.S. de Windt, J.A.A. Hendriks, X. Zhao, L.A. Vonk, L.B. Creemers, W.J.A. Dhert, M. A. Randolph, D.B.F. Saris, Concise review: unraveling stem cell cocultures in regenerative medicine: which cell interactions steer cartilage regeneration and how? Stem Cells Transl. Med. 3 (6) (2014) 723–733.
[37] C.A. Hellingman, W. Koevoet, G.J.V.M. van Osch, Can one generate stable hyaline cartilage from adult mesenchymal stem cells? A developmental approach, J. Tissue Eng. Regen. M. 6 (10) (2012) e1–e11.
[38] F. Gao, Z. Xu, Q. Liang, B. Liu, H. Li, Y. Wu, Y. Zhang, Z. Lin, M. Wu, C. Ruan, W. Liu, Direct 3D printing of high strength biohybrid gradient hydrogel scaffolds for efficient repair of osteochondral defect, Adv. Funct. Mater. 28 (13) (2018) 1706644.
[39] S. Zhao, Z. Xu, H. Wang, B.E. Reese, L.V. Gushchina, M. Jiang, P. Agarwal, J. Xu, M. Zhang, R. Shen, Z. Liu, N. Weisleder, X. He, Bioengineering of injectable encapsulated aggregates of pluripotent stem cells for therapy of myocardial infarction, Nat. Commun. 7 (2016) 13306.
[40] S.P. Pasca, The rise of three-dimensional human brain cultures, Nature 553 (7689) (2018) 437–445.
[41] Z. Cesarz, K. Tamama, Spheroid culture of mesenchymal stem cells, Stem Cell. Int. 2016 (2016) 9176357.
[42] M. Sarem, O. Otto, S. Tanaka, V.P. Shastri, Cell number in mesenchymal stem cell aggregates dictates cell stiffness and chondrogenesis, Stem Cell Res. Ther. 10 (2019) 10.
[43] Y.-S. Hwang, J. Kim, H.J. Yoon, J.I. Kang, K.-H. Park, H. Bae, Microwell-mediated cell spheroid formation and its applications, Macromol. Res. 26 (1) (2018) 1–8.
[44] K. Tachibana, N-cadherin-mediated aggregate formation; cell detachment by Trypsin-EDTA loses N-cadherin and delays aggregate formation, Biochem. Bioph. Res. Co. 516 (2) (2019) 414–418.
[45] B.J. Huang, J.C. Hu, K.A. Athanasiou, Effects of passage number and post-expansion aggregate culture on tissue engineered, self-assembled neocartilage, Acta Biomater. 43 (2016) 150–159.
[46] H. Guo, P.A. Torzilli, Shape of chondrocytes within articular cartilage affects the solid but not the fluid microenvironment under unconfined compression, Acta Biomater. 29 (2016) 170–179.
[47] C. Vinatier, J. Guicheux, Cartilage tissue engineering: from biomaterials and stem cells to osteoarthritis treatments, Ann, Phys. Rehabil. Med. 59 (3) (2016) 139–144.
[48] X.J. Liu, H.Y. Meng, Q.Y. Guo, B.C. Sun, K.H. Zhang, W. Yu, S.C. Liu, Y. Wang, X. G. Jing, Z.Z. Zhang, J. Peng, J.H. Yang, Tissue-derived scaffolds and cells for articular cartilage tissue engineering: characteristics, applications and progress, Cell Tissue Res. 372 (1) (2018) 13–22.
[49] A.R. Armiento, M.J. Stoddart, M. Alini, D. Eglin, Biomaterials for articular cartilage tissue engineering: learning from biology, Acta Biomater. 65 (2018) 1–20.
[50] A.P. Tabatabai, B.P. Partlow, N.R. Raia, D.L. Kaplan, D.L. Blair, Silk molecular weight influences the kinetics of enzymatically cross-linked silk hydrogel formation, Langmuir 34 (50) (2018) 15383–15387.
[51] B.P. Partlow, C.W. Hanna, J. Rnjak-Kovacina, J.E. Moreau, M.B. Applegate, K. A. Burke, B. Marelli, A.N. Mitropoulos, F.G. Omenetto, D.L. Kaplan, Highly tunable elastomeric silk biomaterials, Adv. Funct. Mater. 24 (29) (2014) 4615–4624.
[52] C.J. Little, N.K. Bawolin, X. Chen, Mechanical properties of natural cartilage and tissue-engineered constructs, Tissue Eng. B Rev. 17 (4) (2011) 213–227.
[53] E. Fennema, N. Rivron, J. Rouwkema, C. van Blitterswijk, J. de Boer, Spheroid culture as a tool for creating 3D complex tissues, Trends Biotechnol. 31 (2) (2013) 108–115.
[54] K. Futrega, J.S. Palmer, M. Kinney, W.B. Lott, M.D. Ungrin, P.W. Zandstra, M. R. Doran, The microwell-mesh: a novel device and protocol for the high throughput manufacturing of cartilage microtissues, Biomaterials 62 (2015) 1–12.
[55] A. Goldberg, K. Mitchell, J. Soans, L. Kim, R. Zaidi, The use of mesenchymal stem cells for cartilage repair and regeneration: a systematic review, J. Orthop. Surg. Res. 12 (2017) 39.
[56] C.H. Lee, J.L. Cook, A. Mendelson, E.K. Moioli, H. Yao, J.J. Mao, Regeneration of the articular surface of the rabbit synovial joint by cell homing: a proof of concept study, Lancet 376 (9739) (2010) 440–448.
[57] J.C. Schagemann, H.W. Chung, E.H. Mrosek, J.J. Stone, J.S. Fitzsimmons, S. W. O'Driscoll, G.G. Reinholz, Poly-epsilon-caprolactone/gel hybrid scaffolds for cartilage tissue engineering, J. Biomed. Mater. Res. 93a (2) (2010) 454–463.
[58] J. Luo, J. Meng, Z. Gu, L. Wang, F. Zhang, S. Wang, Topography-induced cell self-organization from simple to complex aggregates, Small 15 (15) (2019) 1900030.
[59] C.-K. Huang, G.J. Paylaga, S. Bupphathong, K.-H. Lin, Spherical microwell arrays for studying single cells and microtissues in 3D confinement, Biofabrication 12 (2) (2020), 025016-025016.
[60] A.M. Delise, R.S. Tuan, Analysis of N-cadherin function in limb mesenchymal chondrogenesis in vitro, Dev. Dynam. 225 (2) (2002) 195–204.
[61] Y. Zhang, H. Mao, C. Gao, S. Li, Q. Shuai, J. Xu, K. Xu, L. Cao, R. Lang, Z. Gu, T. Akaike, J. Yang, Enhanced biological functions of human mesenchymal stem-cell aggregates incorporating E-cadherin-modified PLGA microparticles, Adv. Healthc. Mater. 5 (15) (2016) 1949–1959.
[62] D.R. Albrecht, G.H. Underhill, T.B. Wassermann, R.L. Sah, S.N. Bhatia, Probing the role of multicellular organization in three-dimensional microenvironments, Nat. Methods 3 (5) (2006) 369–375.
[63] E. Potier, N.C. Rivron, C.A. Van Blitterswijk, K. Ito, Micro-aggregates do not influence bone marrow stromal cell chondrogenesis, J. Tissue Eng. Regen. M. 10 (12) (2016) 1021–1032.
[64] G. Bahcecioglu, N. Hasirci, B. Bilgen, V. Hasirci, A 3D printed PCL/hydrogel construct with zone-specific biochemical composition mimicking that of the meniscus, Biofabrication 11 (2) (2019) 13.
[65] J.H. Shim, J.S. Lee, J.Y. Kim, D.W. Cho, Bioprinting of a mechanically enhanced three-dimensional dual cell-laden construct for osteochondral tissue engineering using a multi-head tissue/organ building system, J. Micromech. Microeng. 22 (8) (2012) 11.
[66] S. Camarero-Espinosa, B. Rothen-Rutishauser, E.J. Foster, C. Weder, Articular cartilage: from formation to tissue engineering, Biomater. Sci. 4 (5) (2016) 734–767.
[67] K.A. Athanasiou, A. Agarwal, F.J. Dzida, Comparative study of the intrinsic mechanical properties of the human acetabular and femoral head cartilage, J. Orthop. Res.: official publication of the Orthopaedic Research Society 12 (3) (1994) 340–349.

[68] W. Kabir, C. Di Bella, P.F.M. Choong, C.D. O'Connell, Assessment of native human articular cartilage: a biomechanical protocol, Cartilage (2020), 1947603520973240.
[69] P. Julkunen, T. Harjula, J. Iivarinen, J. Marjanen, K. Seppanen, T. Narhi, J. Arokoski, M.J. Lammi, P.A. Brama, J.S. Jurvelin, H.J. Helminen, Biomechanical, biochemical and structural correlations in immature and mature rabbit articular cartilage, Osteoarthritis Cartilage 17 (12) (2009) 1628–1638.
[70] F. Gao, Z.Y. Xu, Q.F. Liang, B. Liu, H.F. Li, Y.H. Wu, Y.Y. Zhang, Z.F. Lin, M.M. Wu, C.S. Ruan, W.G. Liu, Direct 3D printing of high strength biohybrid gradient hydrogel scaffolds for efficient repair of osteochondral defect, Adv. Funct. Mater. 28 (13) (2018) 13.